Assessing the Ducting Phenomenon and its Potential Impact on GNSS Radio Occultation Refractivity Retrievals over the Northeast Pacific Ocean using Radiosondes and Global Reanalysis

Thomas E. Winning Jr. [1], Feiqin Xie[1] and Kevin J. Nelson[1,a]
[1] Texas A&M University – Corpus Christi, Corpus Christi, 78412, USA
[a] now at: Jet Propulsion Laboratory, California Institute of Technology, Pasadena, 91109, USA
Correspondence to: Thomas E. Winning Jr. (twinning@islander.tamucc.edu)

Abstract. In this study, high-resolution radiosondes from the MAGIC field campaign and ERA5 global reanalysis data are used to assess the elevated ducting layer characteristics along the transect over the northeastern Pacific Ocean from Los Angeles, California to Honolulu, Hawaii. The ~~height of the~~ planetary boundary layer height (PBLH) increases as the strength of the refractivity gradient ~~and resultant ducting decrease from east to west across the analysis~~ decreases westward along the transect. The thickness of the prevailing ducting layer remains remarkably consistent (~110 m) in the radiosonde data. On the other hand, the ERA5 generally resolves the ducting features well but underestimates the ducting height and strength especially over the trade cumulus region near Hawaii. A simple two-step end-to-end simulation is used to evaluate the impact of the elevated ducting layer on RO refractivity retrievals. A systematic negative refractivity bias (*N*-bias) below the ducting layer is observed throughout the transect, peaking (−5.42%) approximately ~~70~~80 meters below the PBL height ~~(-5.42%),~~, and gradually decreasing towards the surface ~~(-~~(−0.5%). ~~Further, the underestimation of the~~ The *N*-bias ~~in the ERA5 data increases in magnitude westward and while the~~ shows strong positive correlation ~~of~~ with the ducting strength. The ERA5 data underestimate the *N*-bias with the ~~minimum gradient and sharpness are all strong; there is no evidence of zonal dependence.~~ magnitude of the underestimation increasing westward along the transect.

Formatted: Font: Italic

Formatted: Font: Italic

Formatted: Font: Italic

Formatted: Font: Times New Roman, 12 pt

1 Introduction

The troposphere, where most weather occurs, consists of two main layers: the planetary boundary layer (PBL) and the free atmosphere (FA) (Garratt, ~~1992~~1994). The PBL characteristics change frequently on both spatial and temporal scales and the PBL height (PBLH) can impact the exchange of heat, momentum, and particulate matter with the FA, making it a critical factor in global energy balances and water cycling (Stull 1988; Ramanathan et al. 1989; Klein and Hartmann 1993). Regular PBL observations are mainly limited to in situ measurements from surface stations and radiosondes. However, spatially and temporally dense in situ PBL observations are only available from field campaigns such as the Boundary Layer Experiment 1996 (BLX96, Stull et al. 1997), the ~~VAMOS~~Variability of the American Monsoon Systems (VAMOS) Ocean-Cloud-Atmosphere-Land Study Regional Experiment (VOCALS-REx, Wood et al. 2011), and the Marine Atmospheric Radiation Measurement (ARM) Global Energy and Water Experiment (GEWEX) Cloud System Studies (GCSS) Pacific Cross Section Intercomparison (GPCI) Investigation of Clouds (MAGIC, Zhou et al. 2015~~), etc.~~). Satellite observations of the PBL are also limited due to signal attenuation of the conventional infrared sounder in the lower troposphere and the low vertical resolution of microwave sounding instruments. Additionally, while the depth of the PBLH can vary from a couple hundred meters to a few kilometers (von Engeln and Teixeira 2013; Ao et al. 2012), the transition layer from the PBL to the FA is typically on the order of tens to hundreds of meters thick (Maddy and Barnet 2008), rendering ineffective PBL sensing from the low vertical resolution passive infrared and microwave sounders.

On the other hand, Global Navigation Satellite System (GNSS) radio occultation (RO) provides global atmospheric soundings with a vertical resolution of approximately 100 m in the lower troposphere under all weather conditions (Gorbunov et al., 2004; Kursinski et al~~.~~., 2000, 1997~~, 2000~~). One of the major GNSS RO missions is the Formosat-3/Constellation Observing System for Meteorology, Ionosphere, and Climate (COSMIC), later referred to as COSMIC-1 (Anthes et al. 2008), and its follow-on mission COSMIC-2 (Schreiner et al. 2020). Numerous studies have documented the high value of GNSS RO for profiling the PBL and determining the PBLH

(Nelson et al. 2021; Winning et al. 2017; Ho et al. 2015; Ao et al. 2012; ; Guo et al. 2011; Basha and Ratnam 2009; Ao et al. 2008; Xie et al. 2008).

The advancement of the GNSS RO technique with open-loop tracking (Sokolovskiy et al., 2006; Beyerle et al., 2003; Ao et al., 2003) along with the implementation of the radio-holographic retrieval algorithm (Jensen et al., 2004; Jensen et al., 2003; Gorbunov, 2002) have led to much improved PBL sounding quality. However, probing the marine PBL remains challenging as systematic negative biases are frequently seen in RO refractivity retrievals (Feng et al. 2020; Xie et al. 2010). One major cause of the refractivity bias (hereafter *N*-bias) is the RO retrieval error due to elevated atmospheric ducting often seen near the PBLH (Ao et al., 2007; Xie et al., 2006; Ao et al. 2003; Sokolovskiy 2003~~,~~). This elevated ducting prevails over the subtropical eastern oceans (Feng et al., 2020; Lopez, 2009; von Englen et al., 2003~~; Lopez, 2009, Feng et al., 2020~~), and the horizontal extent of ducting in these regions can be on the order of thousands of kilometers (Winning et al. 2017; Xie et al. 2010). In the presence of ducting, the vertical refractivity gradient exceeds the critical refraction threshold for L-band frequencies (i.e., $dN/dz \leq -157$ N-units km^{-1}). The steep negative refractivity gradient is often observed in the vicinity of the PBLH, which is typically caused by an atmospheric temperature inversion, a sharp decrease in moisture ~~lapse~~, or a combination of both. When ducting is present, the Abel inversion (e.g., Fjeldbo et al., 1971) in the standard retrieval process encounters a non-unique inversion problem due to a singularity in the bending angle, resulting in large, systematic underestimation of refractivity (*N*) below the ducting layer (Xie et al. 2006; Ao et al., 2003; Sokolovskiy, 2003~~; Ao et al., 2003; Xie et al. 2006~~). The large uncertainty in RO refractivity coupled with the singularity in bending angle hinders assimilation of RO observations into numerical weather models, resulting in discarding of a significant percentage of RO measurements inside the PBL (Healy, 2001).

~~In order to thoroughly evaluate the N-bias attributed to ducting, the issue must be examined from the ground up by using a dense collection of observations where the occurrence of ducting in the lower troposphere is present in the daily climatology of the region. Section 2 provides details of the two data sets used for this study: high-resolution radiosondes over the northeastern Pacific Ocean and ERA5 reanalysis profiles colocated to the radiosondes. Additionally, we discuss the method used for colocation between the radiosondes and ERA5 profiles, as well as detection of the ducting layer and the corresponding PBLH. Section 3 presents the ducting climatology for~~

Formatted: Font: Italic

~~key variables, such as ducting height, PBLH, minimum N-gradient, and gradient sharpness. The characteristics of ducting including the thickness and strength along the cross-section are also shown. Furthermore, we evaluate the ducting-induced N-bias in GNSS RO refractivity retrievals by carrying out a two-step end-to-end simulation. Section 4 summarizes the findings and discusses the direction of future research.~~

~~2 Data and methods~~

~~**2.1 MAGIC radiosonde and colocated ERA5 data sets**~~To comprehensively assess the potential impact of ducting on GNSS RO retrievals, we begin by constructing a detailed ground truth of PBL ducting statistics. This is derived from an extensive set of high-resolution radiosonde data over the northeastern Pacific Ocean, a region known for prevailing ducting conditions. Subsequently, we conduct a simulation study using the radiosonde data to evaluate the *N*-biases caused by varying ducting characteristics. Section 2 provides details of the two data sets used for this study: high-resolution radiosondes over the northeastern Pacific Ocean and the colocated ECMWF Reanalysis version 5 (ERA5, Hersbach et al. 2020) profiles. Additionally, we discuss the co-location criteria and the detection method for ducting layer and the corresponding PBLH. Section 3 presents the ducting statistics for key variables, such as ducting height, PBLH, minimum refractivity gradient, and sharpness parameter. The characteristics of ducting including the thickness and strength along the cross-section are also shown. Furthermore, we evaluate the ducting-induced *N*-bias in GNSS RO refractivity retrievals by carrying out a two-step end-to-end simulation. Section 4 summarizes the findings and discusses the direction of future research.

2 Data and methods

2.1 MAGIC radiosonde and colocated ERA5 data

A collection of high-resolution radiosondes from the Marine Atmospheric Radiation Measurement (ARM) GCSS Pacific Cross Section Intercomparison (GPCI) Investigation of Clouds (MAGIC) are utilized as the primary data set in this analysis (Lewis 2016; Zhou et al. 2015). The MAGIC field campaign took place from 26 September 2012 to 2 October 2013 as part of the U.S Department of Energy ARM Program Mobile Facility 2 (AMF2) aboard the Horizon Lines container ship, *Spirit*, which completed 20 round trip passes between Los

Angeles, California and Honolulu, Hawaii during the yearlong data collection period (Painemal et al., 2015; Zhou, 2015). During each transit, radiosondes were launched at 6-hour intervals from the beginning of the program through the end of June 2013; the observation frequency increased to every 3 hours from July 2013 through the end of the campaign (Zhou et al., 2015). A total of 583 MAGIC radiosonde profiles were collected during the field campaign (Zhou et al., 2015), all with a vertical sampling frequency of 0.5 Hz (2 seconds), which provides an average vertical ~~sampling interval~~resolution of ~8 m below 3 km, but varies due to local vertical motion. ~~The number of observations and location (Fig. 1)~~Use of this data set serves multiple benefits. First, the northeast Pacific transitions from a shallow stratocumulus-topped PBL to a higher, trade-cumulus boundary layer regime along the GPCI transect (Garratt, ~~1992); this unique transition zone provides an ideal natural laboratory for studying the horizontal variation of the marine PBL.~~1994). Second, the large number of observations over a 12-month time frame provides high temporal (diurnal and seasonal) and spatial profiling of the PBL along the GPCI transect~~.~~ seen in Fig.1. Finally, ducting is prevalent throughout the domain ~~over which the observations were captured~~ which creates ~~an opportunity to perform an analysis over~~ a natural cross-section of refractivity field in X (zonal) and Z (vertical) dimensions.

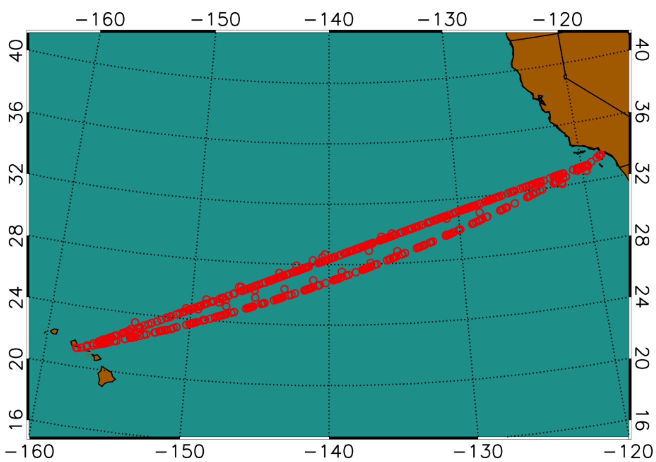

Figure 1: Location of radiosonde observations from the MAGIC field campaign October 2012~~-~~–September 2013.

~~The radiosonde profiles are colocated with the ECMWF Reanalysis version 5 (ERA5, Hersbach et al. 2020). The ERA5 reanalysis data have a horizontal grid resolution of 0.25˚x0.25˚, 1-hour temporal resolution, and 137 vertical levels from the surface to 0.01 hPa (Hersbach et al., 2020). An average of 19 model levels exist below 1 km providing the highest vertical resolution near~~

the surface; vertical density of the model decreases with height to 8 levels within the 1 km-2 km layer and further decreasing to 5 levels within the 2 km-3 km. Each MAGIC radiosonde profile was colocated with the nearest ERA5 grid point that is within 1.5 hours of the closest 3-hourly model reanalysis profile.

2.2 PBL height detection with the minimum gradient method

At GNSS L-band frequencies, the atmospheric refractivity (*N* in N-units) is derived from the refractive index *n*, where *N*= (*n*-

The radiosonde profiles are colocated with ERA5 model reanalysis profiles. The ERA5 reanalysis data have a horizontal grid resolution of 0.25˚x0.25˚, 1-hour temporal resolution, and 137 uneven vertical model levels from the surface to 0.01 hPa. The model level density decreases with height: on average, there are 19 model levels below 1 km (10 –100 m resolution), which reduces to 8 levels between 1 and 2 km (100 – 160 m resolution), and further reduces to 5 levels between 2 and 3 km (160-200 m resolution). Each MAGIC radiosonde profile was colocated with the nearest ERA5 grid point that is within 1.5 hours of the closest 3-hourly model reanalysis profile.

2.2 PBL height detection with the minimum gradient method

At GNSS L-band frequencies, the atmospheric refractivity (*N* in N-units) is derived from the refractive index *n*, where $N = (n - 1) \times 10^6$ and, in the neutral atmosphere (Kursinski et al., 1997), is a function of the atmospheric pressure (*P* in mb), temperature (*T* in K), and partial pressure of water vapor (P_w in mb) as seen in Eq. (1) from Smith and Weintraub (1953).

$$N = 77.6\frac{P}{T} + 3.73 \times 10^5 \frac{P_w}{T^2}, \qquad (1)$$

Atmospheric refractivity decreases exponentially with height which, all else being equal yields a negative value vertical gradient. As such, the minimum refractivity describes the largest magnitude value.

Over the subtropical eastern oceans, a sharp decrease in moisture is often associated with a strong temperature inversion marking a clear transition from the PBL to the FA. Both the distinct decrease in moisture lapse and the temperature inversion lead to a sharp negative refractivity gradient which can be precisely detected from GNSS RO. Numerous studies have implemented the simple minimum gradient method to detect the PBLH, which isi.e., the locationheight of the minimum refractivity gradient (Ao et al., 2012; Seidal et al., 2010; Xie et al., 2006). When the vertical refractivity gradient is less than the critical refraction (dN/dz ≈ −157.0 N-units km^{-1}), ducting occurs (Sokolovskiy, 2003). To betterTo assess the strength of the refractivity gradient for more robustrobustness of PBLH detection with gradient method, Ao et al. (2012) introduced the sharpness parameter, which is defined ($\tilde{N}'$) to measure the relative magnitude of the minimum gradient from surface to 5 km as the ratio of the minimum vertical refractivity gradient to the root mean square error of the refractivity gradient profile (eq. 2).follows:

$$\tilde{X}' \equiv -\frac{X'_{min}}{X'_{RMS}} \tilde{N}' \equiv -\frac{N'_{min}}{N'_{RMS}}, \quad (2)$$

Each refractivity gradient profile can then be filtered to identify the PBLH values with sharpness parameter exceeding certaina specific threshold, thus increasing the robustness of PBLH detection. In this study, the MAGIC radiosonde refractivity profiles were first interpolated to a uniform 10 m vertical grid and then smoothed by a 100 m boxcar window to reduce the noise in the N gradient profile that is a result of resulting from the high sampling rate. Moreover, the 100 m smoothed radiosonde will be more consistent with the vertical resolution of GNSS RO measurements (e.g. Gorbunov et al., 2004). Colocated ERA5 data were also vertically interpolated to the same 10 m grid but not smoothed as these data do not contain the inherent noise as the radiosonde observations. In addition, as the elevated ducting layer is the focus of this study, the lowest 0.3 km above mean-sea-level of the *N*-profile near surface are excluded (e.g., Xie et al., 2012). Subsequently, the height of the minimum refractivity gradient (within 0.3 km and 5 km) will be identified as the PBLH.

2.3 Ducting layers

When the vertical refractivity gradient is less than the critical refraction (d*N*/dz ≈ −157.0 *N*-units km^{-1}), ducting occurs (Sokolovskiy, 2003). A ducting layer is identified as any interval of continuous points with a vertical refractivity gradient equal to or less than −157 N-units km^{-1}. Instances of multiple ducting layers occurring within a profile are present foinfor both the MAGIC (31.5%) and ERA5 (6.7%) data sets. A ducting layers is identified as any interval of continuous points with refractivity gradient equal to or less than −157 N-units km^{-1}. Note, howeverIn this study, we only refer to the "ducting layer" of each profile as therecognize one dominant “ducting layer corresponding to the layer in which” in each profile where the minimum vertical gradient is located (.Fig. 2a-d). The ducting layer thickness (Δh) is defined as the interval between the top and bottom of the ducting layer where the N refractivity gradients reach critical refraction. Similarly, the strength of each ducting layer (ΔN) is defined as the refractivity difference between the bottom and top of the ducting layer. The ducting layer height is in reference to the top of the ducting layer (Ao, 2007), which is generally slightly above the PBLH.

Figure 2 illustrates two ducting layers in a representative MAGIC radiosonde case near -150°, but only one in the colocated ERA5 profile. Profiles of radiosonde shows vertical profiles of refractivity (deca *N*-units, da*N* x 1/10, *N/10*), temperature (*T*)), and specific humidity (*q*) andalong with their respective vertical gradients (d*N*/dz, d*T*/dz and d*q*/dz) are shown in from a representative MAGIC radiosonde (Fig. 2a and ,b) case located at (23.69°N, −150.02°E), and its colocated ERA5 (Fig. 2b, respectively. Similar plots for the collocated ERA5 profiles are shown in Fig. 2c and Fig. 2d.,d) profile at (23.75°N, −150.00°E). The PBLH of the radiosonde (2.10 km) is almost identical to the colocated ERA5 (2.14 km) and the “dominant” ducting layer near the PBLH demonstrates similar thickness. However, a second, weaker ducting layer seen in the radiosonde above the PBLH was not captured by the ERA5. This is likely due to the lower vertical resolution in ERA5 as can be seen in the gradient plots (Fig. 2b and Fig. 2d).

It is also worth noting that the residual layer between 1.2-1.5 km with gradient close to critical refraction is seen in the radiosonde is also seen in the ERA5 profile, but at a much lower altitude (~0.7 km).

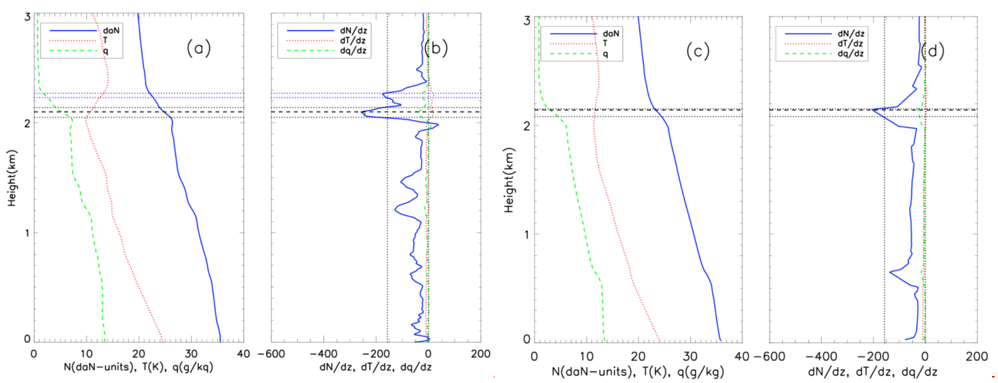

Formatted: Font: Italic

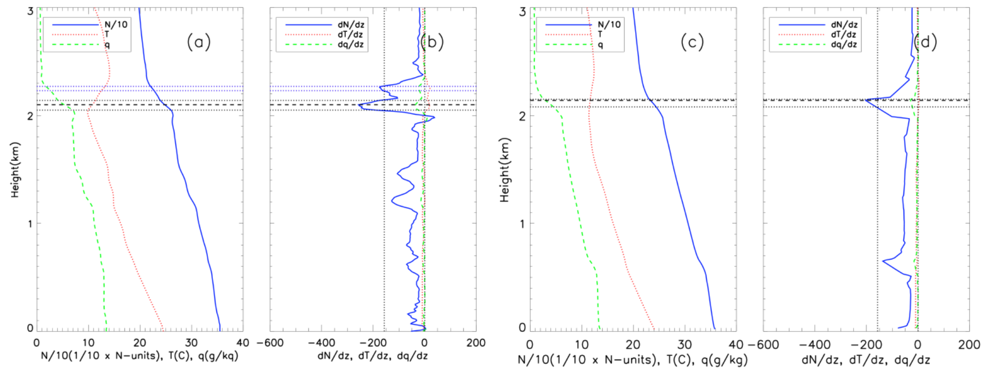

Figure 2: ~~(a) MAGIC radiosonde (-150.00°) and (c) colocated ERA5 (-150.00°)~~Vertical profiles of refractivity (~~*daN*~~1/10 x N in *N*-units, *N/10*, solid blue), temperature (*T* in ~~K~~°C, dotted red) and specific humidity (*q* in g kg^{-1}, dashed green~~); (b) the~~) for (a) radiosonde at (23.69°N, -150.02°E) launched at 2012-10-02, 05:30 UTC, and (c) colocated ERA5 at (23.75°N, -150.00°E); and associated ~~radiosonde and (d) ERA5~~ gradient profiles~~.~~ for radiosonde (b) and ERA5 (d). The horizontal dashed line highlights the height of the minimum gradient, i.e., PBLH. The paired horizontal dotted lines represent the bottom and top of the two ducting layers in the radiosonde profile~~,~~ (a and b) but only one in the ERA5 profile~~.~~ (c and d).

2.4 Evaluation of GNSS RO *N*-bias resulting from ducting

Formatted: Font: Italic

In order to estimate the systematic negative *N*-bias in GNSS RO observations in the presence of ducting, we use an end-to-end simulation on the radiosonde and ERA5 refractivity profiles. The simulation consists of a two-step process adapted from Xie et al. (2006). The first step is to simulate the 1-~~dimentional~~dimensional GNSS RO bending angle as a function of impact parameter (i.e., the product of refractive index and the radius of the Earth's curvature) by forward Abel integration of an input refractivity profile assuming a spherically symmetric atmosphere~~.~~ (Sokolovskiy, 2001; Eshleman, 1973, Fjeldbo and Eshleman, 1968). The second step is to simulate the GNSS RO refractivity retrieval by applying the Abel inversion on the simulated bending angle from step one. In the absence of ducting, the impact parameter ~~(i.e., the product of refractive index and the radius of the curvature) decreases~~increases monotonically with height, allowing a unique solution to the inverse Abel retrieval that is the same as the original refractivity profile input. However, in the presence of an elevated ducting layer, the Abel retrieval systematically underestimates the refractivity profile due to the non-unique Abel inversion problem resulting from the singularity in bending angle across the ducting layer (Xie et al., 2006; Sokolovskiy 2003~~;~~). ~~Xie et al., 2006).~~ It should be noted that after the 100 m vertical smoothing on radiosonde (no smoothing on ERA5) profiles as described in section 2.2, an additional 50 m vertical smoothing has been applied to the simulated bending angle profiles of

Formatted: Font: Italic

both radiosonde and ERA5 data sets to alleviate the challenge of integration through the very sharp bending angle resulting from ducting in the inverse Abel integration procedure (Feng et al., 2020).

Figure 3 shows the end-to-end simulation results for the same radiosonde (a~~-~~–d) and the colocated ERA5 (e~~-~~–h) cases from Fig. 2. Figures 3a and 3e show ~~the input~~ refractivity ~~profile~~profiles from the radiosonde (N_{rds}), and the colocated ERA5 (N_{ERA5}) ~~and~~data as well as their corresponding Abel refractivity ~~retrieval~~retrievals (N_{Abel}~~), respectively.~~). The PBLH is marked by a horizontal dotted line. The peak bending angle is consistent with the sharp refractivity gradient. Figure 3b shows the fractional *N*-bias between the simulated Abel retrieved RO refractivity profile and the observation, i.e., ((N_{Abel} ~~-~~ – N_{Obs})/N_{Obs}~~)*100%.~~). Considering the significant spatial and temporal variations of ducting height along the transect, each *N*-bias profile is normalized to its PBLH for the purposes of comparison. For example, the zero-adjusted height refers to the PBLH for each individual profile. The systematic negative *N*-bias is clearly shown below the ducting layer marked by the PBLH in both cases, with the biases decreasing at lower altitude, the largest magnitude bias ~~(~~(–5% for radiosonde; ~~-~~–2.5% for ERA5) close to the ducting height and a minimum magnitude approaching zero near the surface.

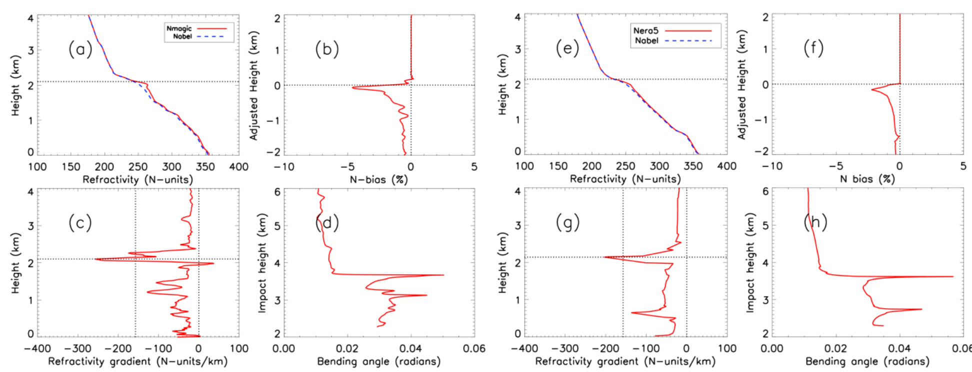

Figure 3: ~~Four-panel comparison of individual profiles of N_{Obs} vs. N_{Abel} that are reconstructed through the end~~End-to-end simulation~~. Four panels~~ data for MAGIC ~~of~~radiosonde launched at 0530 UTC on 20121002 showing: (a) N_{Obs} (solid red) and N_{Abel} (blue dashed) from surface to ~~10~~4 km; (b) PBLH adjusted *N*-bias ((N_{Abel} ~~–~~– N_{Obs})/N_{Obs}~~)/ N_{Obs})*100%;~~); (c) ~~minimum~~refractivity gradient and (d) bending angle vs. impact parameter. ~~Colocated ERA5 profiles are~~The same is shown in panels e-h~~, respectively~~ for the colocated ERA5 profile.

~~3~~ 3 Analysis

~~Out of a total of 583 MAGIC~~Quality control for radiosonde (and ~~co-located~~colocated ERA5) profiles~~, quality control has been implemented~~ was based on five key criteria. First, a total of 19

Formatted: Font: Not Italic
Formatted: Font: Not Italic
Formatted: Font: Italic
Formatted: Font: Italic
Formatted: Font: Italic
Formatted: Font: Italic
Formatted: Normal, No bullets or numbering

radiosonde and 24 ERA5 profiles near the southern California coast were removed due to ~~a zonal position~~their positions east of ~~-120°~~ −120°E or anomalously high PBL ~~heights~~ (PBLH > 3.0 km) with no distinct minimum gradient. The remaining profiles in the easternmost portion of the domain were too few in number to calculate meaningful statistics. Second, any profile lacking critical refraction (i.e. d*N*/dz < ~~-~~ −157 N-units km^{-1}) points was excluded from the analysis which resulted in the removal of 47 radiosonde and 176 ERA5 profiles. Third, the noisy bending angle could result in errors in Abel refractivity retrieval and cause positive *N*-bias. Therefore, the profiles with *N*-bias greater than +0.5% are excluded resulting in the removal of 61 MAGIC profiles and 16 ERA5 profiles. Fourth, the profiles with only surface ducting ~~are discarded when the only refractivity gradient less than -157 N-units km^{-1} occurs~~, i.e., below ~~the~~ 300 m threshold, are discarded. Finally, 25 radiosonde profiles and 2 ERA5 profiles were removed due to the Abel retrieval failure. After implementing all quality control measures, the number of radiosonde and ERA5 profiles used for the *N*-bias analysis is reduced to 396 and 319 profiles, respectively.

3.1 PBL ~~climatology~~analysis

To evaluate the ducting ~~climatology~~properties along the transect from the coast of southern California to Hawaii, we group the MAGIC radiosonde and the colocated ERA5 profiles into eight 5° longitude bins between ~~-160.0° and -120.0°. The equally spaced bins are centered at -157.5°, -152.5°, -147.5°, -142.5°, -137.5°, -132.5°, -127.5° and -122.5°~~ −160.0° and −120.0°, which allows for the spatial variation of the PBL, ducting layer and the associated properties along the transect to be easily illustrated. Figure 4 shows the median value of PBLH (a), ~~sharpness (b) and~~ minimum gradient (b) and sharpness parameter (c) along the transect. The median-absolute-deviation (MAD) for each parameter is also shown.

In Fig. 4a, the MAGIC radiosondes clearly show the gradual increase of the PBLH along the transect from the shallow stratocumulus-topped PBL (~800 m) near the southern California coast westward to the much deeper trade-cumulus regime (~1.8 km) near Hawaii. A similar structure is seen in the colocated ERA5 data but with an average low bias of 165 m below the radiosonde. However, a nearly 800 m underestimation in PBLH over the two westernmost bins near Hawaii is also seen, this is consistent with what is found over the equivalent trade cumulus region of the subtropical southeast Pacific Ocean (Xie et al., 2012). Such a discrepancy could be due to the sensitivity of gradient method to the vertical resolution of the data. Over the western segment of

Formatted: Font: Italic

Formatted: Font: Italic

Formatted: Font: Italic

Formatted: Font: Italic

the transect (near Hawaii), two major gradient layers (one at ~1 km and the other at ~2 km) with comparable refractivity gradients are often observed (e.g., Fig. Such a discrepancy could be due to the decreasing vertical resolution with height in the ERA5 profiles. This results in a sharper refractivity gradient caused by the frequent residual layer (below 1 km) as compared to the actual PBLH near 2 km.2). The gradient layer at around 2 km is well-known as the trade-wind inversion. While the lower-level gradient layer at ~1 km, is generally called a mixing layer. Note the radiosonde data exhibit consistent vertical sampling (~8 m resolution) below 3 km, and resolve both layers well. However, the ERA5 data have an uneven vertical sampling intervals increasing with height, with 10 – 100m resolution below 1 km, 100 – 160 m within 1-2 km, and 160 – 200 m within 2-3 km. Therefore, the ERA5 data are more likely to resolve the sharp gradient structure below 1 km than the one at higher altitude. This could result in resolving the mixing layer (below 1 km) with the sharpest refractivity gradient, instead of the trade-wind inversion near 2 km in the ERA5 data. Note that the larger median absolute deviation for the westernmost bins compared to the rest of the transect illustrates the existence of greater PBLH variability closer to the trade-cumulus-topped boundary layer.

regime. The westward decreasing magnitude of the minimum refractivity gradient (Fig. 4b) and sharpness parameter (Fig. 4c) indicates the westward weakening of moisture lapse rate and/or temperature inversion across the PBL top, which is consistent with the decreasing synoptic-scale subsidence from the California coast to Hawaii. (Riehl, 1979).

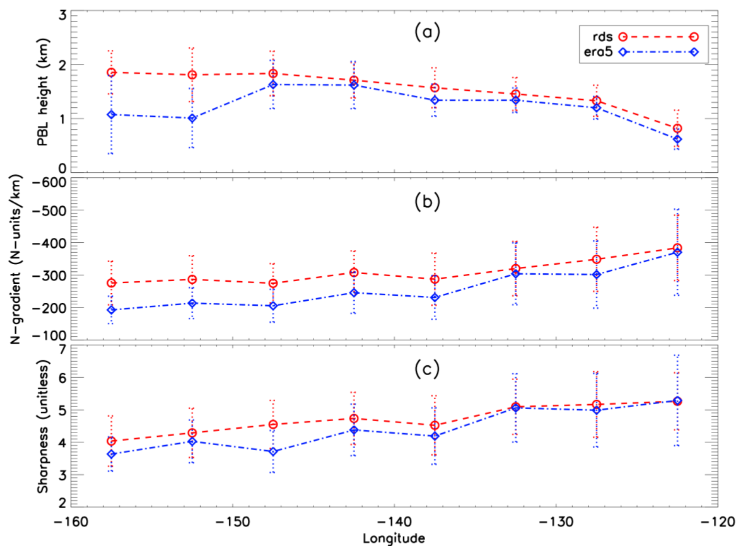

Figure 4: Zonal transect of 5˚ bin MAGIC and ERA5 ~~(a)~~ PBLH~~, (b) sharpness parameter and (c)~~ (a), minimum refractivity gradient (b) and sharpness parameter (c) for MAGIC (median in red circle and dashed line, MAD in ~~dashed~~red dotted error bars) and ERA5 (median in blue diamond~~, MAD in~~ and dot-dashed line, MAD in blue dotted error bars).

Formatted: Font: 12 pt, Not Bold

Formatted: Line spacing: 1.5 lines

It is also notable that the ERA5 ~~systemically~~systematically underestimates not only the PBLH~~,~~ but also the magnitude of the minimum ~~N~~ gradient across the entire transect~~; this~~. This can also be seen in the sharpness parameter west of -–132.5˚. This discrepancy could ~~again~~ be partially attributed to the decrease in vertical sampling in ERA5 profiles as compared to the radiosondes, the result of which leads to a weaker PBL ~~N~~ refractivity gradient and coincides with an increasing PBLH. Therefore, the underestimation of the ERA5 minimum ~~N~~ refractivity gradient increases in magnitude from east to west and becomes most prominent near Hawaii where the PBLH reaches the maximum height over the region.

3.2 Ducting ~~climatology~~characteristics

As introduced in Sect. 2.3, the key characteristics of the ducting layer along the transect will be investigated, these include the ducting layer height, thickness (Δ*h*), and strength (Δ*N*), as well as the average refractivity gradient within the ducting layer (Δ*N*/Δ*h*). All parameters are interpolated to a 10 m vertical grid.

The ducting layer heights from both radiosonde and ERA5 show a westward increase along the transect ~~(Fig. 5a), which~~ is ~~similar to the PBLH~~seen in Fig. ~~4a~~5a. Note again that the ERA5 shows a systematic ~100-–200 m low bias when compared to the radiosondes between -–122.5˚ and -–147.5˚, with the difference increasing to more than 500 m near Hawaii.

The ducting layer thickness is the median height from the bottom of the ducting layer to the top and is expressed in km (Fig. 5b). Ducting thickness (Δ*h*) for MAGIC shows a near constant value of 110 m across the entire transect with only a slight increase to 130 m at -–122.5˚~~; this is~~, consistent with ~~findings from~~ Ao et al. (2003). Conversely, the ERA5 shows a constant but slightly thicker ducting layer to the east of -–137.5˚ and then a decreasing thickness to the west of -–137.5˚ (Fig. 5b).

The ducting layer strength is the decrease in refractivity from the bottom of the ducting layer to the top (Fig. 5c) and the ratio Δ*N*/Δ*h* reflects the average gradient of the ducting layer (Fig. 5d). The ducting strength (Δ*N*) for the radiosondes generally ranges from 25 N-units near Hawaii to 40 N-units near the coast of California. Both Δ*N* and Δ*N*/Δ*h* show an overall westward decreasing trend along the transect which is consistent with the decrease in magnitude of the ~~N-~~refractivity gradient (Fig. 4b). Note that MAGIC and ERA5 show similar ducting strength in the eastern part of the region but diverge near ~~-~~–137.5° with ERA5 10 to 20 N-units weaker than the MAGIC profiles. On the other hand, ERA5 shows a systematic lower average refractivity gradient ($\Delta N/\Delta h$) than MAGIC throughout the transect, indicating the challenge in ERA5 to consistently resolve the sharp vertical structure in refractivity, and likewise in temperature and moisture profiles, across such a thin ducting layer. The problem becomes acutely clear near the trade cumulus region.

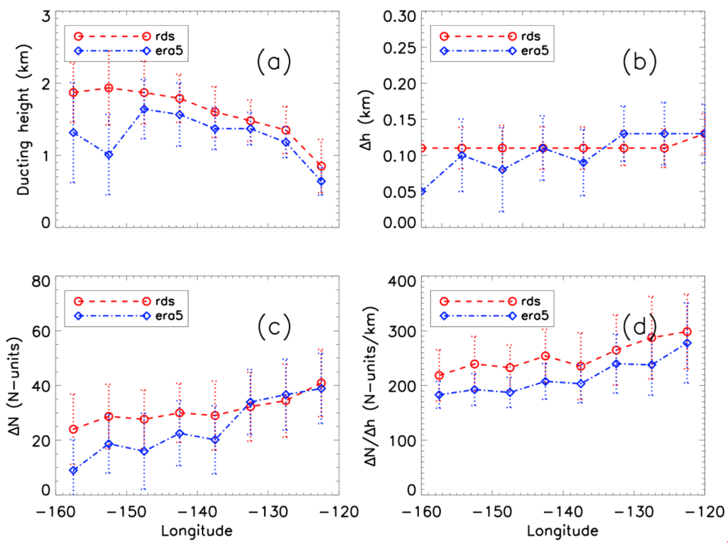

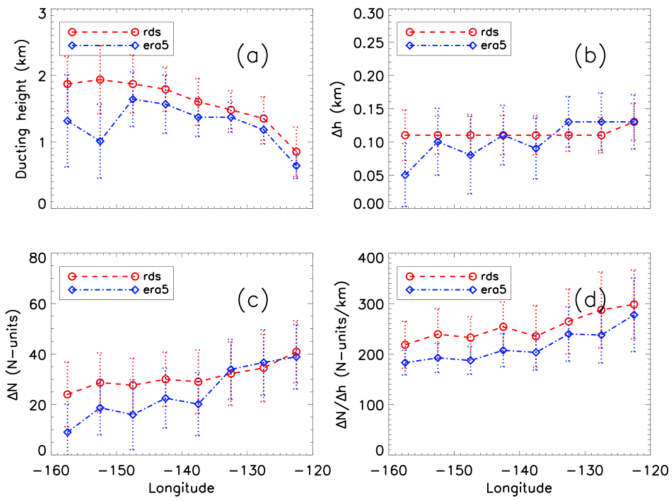

Figure 5: Zonal transect of 5° bin median (a) ducting height, (b) ducting layer thickness (Δh), (c) ducting layer strength (ΔN), and (d) average ducting layer gradient $\Delta N/\Delta h$ for MAGIC (median in red circle and red-dashed line, MAD in red-dotted error bars) and ERA5 (median in blue diamond and dot-dashed ~~error bars~~line, MAD in blue-dotted error bar).

Figure 6 shows ducting layer thickness as a function of ducting layer strength, with each data point colored by its respective longitude bin. The relationship between Δh and ΔN is not longitude-dependent for either data set, but a linear trend is evident for thinner ducting layers (Δh < 0.1 km) with weaker ducting strength (ΔN < ~25 N-units). However, for the ducting layers thicker than ~~the median value of~~ 0.1 km, such a trend becomes less identifiable, and the ducting strength ΔN begins to show more variability toward larger values.

Formatted: Font: 9 pt, Bold

Formatted: Justified, Line spacing: single

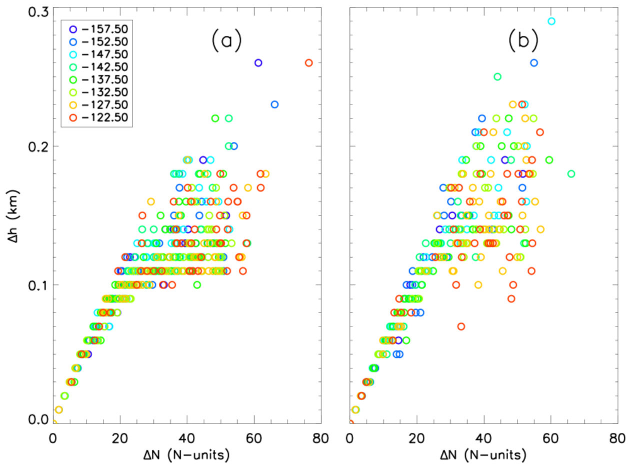

Figure 6: Comparison of individual profiles' ducting strength (Δ*N*) vs. ducting thickness (Δ*h*) for MAGIC (a) and ERA5 (b). The color of each circle represents the location of the 5° longitude bin of each observation.

3.3 Ducting-induced GNSS RO *N*-bias statistics

Formatted: Font: Italic

To estimate the systematic negative *N*-bias in GNSS RO observations due to ducting, we have applied the end-to-end simulation described in sect. 2.4 to all radiosonde and ERA5 refractivity profiles with at least one elevated ducting layer detected~~ (details in Sect. 2.5).~~. The *N*-bias ~~climatology~~ along the transect as well as its relationship to the ducting properties are presented below.

Formatted: Font: Italic

Formatted: Font: Italic

3.3.1 Assessing ducting-induced *N*-bias~~ climatology~~

Formatted: Font: Italic

Figure 7 shows a composite of both MAGIC (396 profiles) and ERA5 (319 profiles) *N*-bias profiles which have been normalized to their PBLH, with the median *N*-bias and MAD overlaid. The ~~comparison reveals a number of occurrences of multiple ducting layers above the minimum gradient identified PBL in the MAGIC data while there are significantly less occurrences in the ERA5 data. Figure 7 illustrates the systematically~~systematic negative *N*-bias peaks at ~~nearly~~approximately 100 m below the PBLH ~~(ducting height)~~ and decreases at lower ~~altitudes. Many radiosonde profiles show smaller negative N-biases above the PBLH (e.g., zero adjusted height), but only a few in ERA5 which is a result of the secondary ducting layers above the major ducting layer near PBLH.~~ altitude. The peak median value of the *N*-bias for radiosondes is ~~-~~–5.42% (MAD, 2.92%), nearly twice the ERA5 value of ~~-~~–2.96% (MAD, 2.59~~%). It is worth~~

Formatted: Font: Italic

Formatted: Font: Italic

Formatted: Font: Italic

Formatted: Font: Italic

~~noting that~~ %), indicating the significant underestimation of ducting strength in ERA5 data. However, the variabilities (MAD) ~~between~~of the radiosonde and ERA5 data are ~~very close to~~ within 0.33% of each other, indicating that ERA5 data successfully capture the variations of ducting features seen in the radiosondes. It is worth noting that many radiosonde profiles show small negative *N*-biases above the PBLH (i.e., zero-adjusted height), which is the result of a secondary ducting layer above the major ducting layer near the PBLH. Conversely, few ERA5 profiles show the presence of the secondary ducting layer above PBLH.

~~A closer look at each data set reveals that the difference between the 5°median PBLH and height of the maximum N-bias (h_{PBL}-$h_{N\text{-}bias}$) is positive for all bins. The maximum difference of 100 m is located in bin -137.5° and a minimum difference of ~15 m at bin 152.5°. Comparatively, the ERA5 reflects a PBL height greater than the N-bias height for each bin with a maximum difference of 230 m located at -142.5° and a minimum of ~45 m at -157.5°. The ERA5 data show a larger average height difference between the PBL and N-bias (120 m) than the radiosonde data (70 m).~~

~~The N-bias comparison of the 5° bin median values of the two data sets favors the radiosonde data with smallest magnitude difference located at bin -147.5° (-4.37%) and largest magnitude difference of -7.86% located at bin -122.5°. Comparatively, the ERA5 minimum N-bias difference of -0.77% (-157.5°) is much lower than the radiosonde while the maximum difference is similar in both magnitude (-5.92%) and location (-122.5°).~~

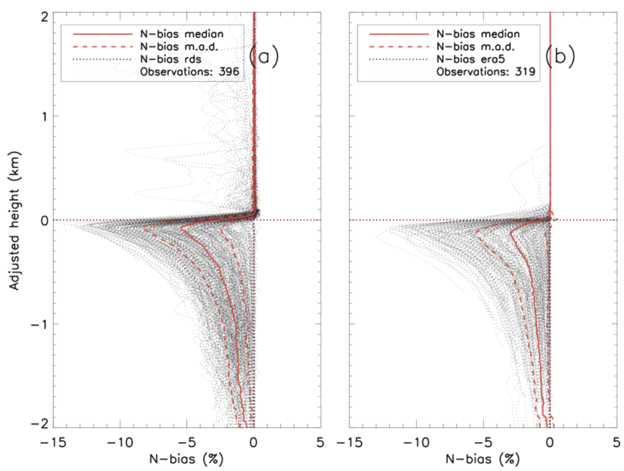

Figure 7: Fractional refractivity difference (*N*-bias~~)~~ in %) between the simulated Abel-retrieved refractivity profile and the original observation profile ((N_{Abel} – N_{Obs})/N_{Obs}~~)*100%,~~), for all individual observations (dotted gray): (a) MAGIC

Formatted: Font: Italic

radiosondes (396 total profiles) and (b) ERA5 (319 total profiles) with population median (solid red) ± MAD (dashed red). Note the zero value in the adjusted height refers to the PBLH for each individual *N*-bias profile.

3.3.2 Zonal variation of the *N*-bias along the transect

To illustrate the large variation in the *N*-bias vertical structure resulting from the spatial ~~variation~~variations of ducting height and strength, ~~we separately present~~Fig. 8 presents the *N*-bias profiles (median ± MAD) for each 5˚ bin, replacing the zero adjusted height with the median PBLH for each bin~~ (Fig. 8).~~. The radiosonde composite (Fig. 8a) illustrates the westward transition of the median *N*-bias ~~height~~profiles from ~~1.8 km~~the largest peak *N*-bias at ~~Honolulu, HI to~~ ~0.8 km near the coast of Los Angeles, ~~CA.~~California, to a much reduced peak *N*-bias but higher altitude of ~1.8 km at Honolulu, Hawaii. Table 1 ~~provides supplemental~~ lists detailed statistics of the peak *N*-bias values at each bin for ~~the Fig. 8 illustration of the~~ both radiosonde and ERA5 ~~statistical climatology.~~ data. Although the vertical structure of the *N*-bias profiles along the transect are consistent as seen in Fig. 7, significant changes of the *N*-bias magnitude and its peak *N*-bias occurring height along the transect are clearly seen.

The maximum peak *N*-bias (−7.86%) in the radiosonde ~~N-bias variation shows a~~ data is located at the easternmost of the transect near California (−122.5˚E). Whereas the minimum ~~magnitude of~~peak *N*-bias (−4.37%) is located near the center of the transect ~~and two of the largest magnitude~~(−147.5˚E). Similarly, the ERA5 also show the maximum peak *N*-bias (−5.92%) near California (−122.5˚E). However, the minimum peak *N*-bias (−0.77%) is found near Hawaii (−157.5˚E). Overall, the *N*-bias in ERA5 are smaller than radiosonde in all bins. However, a noticeable difference ~~values of as the bookends while the ERA5 N-bias values have a larger range but peak values (-5.41% to -6.23%) in the three bins closest to California; note the significantly reduced peak N-bias to the west of -137.5˚ (-3.10% to -0.71%). Moreover, a discontinuity~~ exists ~~in~~between the ERA5 and radiosonde profiles for the two westernmost longitude bins ~~(-~~(−157.~~5˚~~5˚E and ~~-~~−152.~~5˚) which show a markedly~~5˚E) where the ERA5 reveals a much lower and weaker *N*-bias~~.~~ than the MAGIC data.

Note that the PBLH is above the height of the peak *N*-bias, with a maximum difference of 100 m (−137.5˚E) and a minimum difference of ~15 m (−152.5˚E). Comparatively, the ERA5 PBL height shows greater difference than the height of peak *N*-bias with a maximum difference of 230 m (−142.5˚E) and a minimum of ~45 m (−157.5˚E).

Formatted: Font: Italic

Formatted: Font: Italic

Formatted: Font: Italic

Formatted: Font: Italic

Formatted: Font: Italic

Formatted: Font: Italic

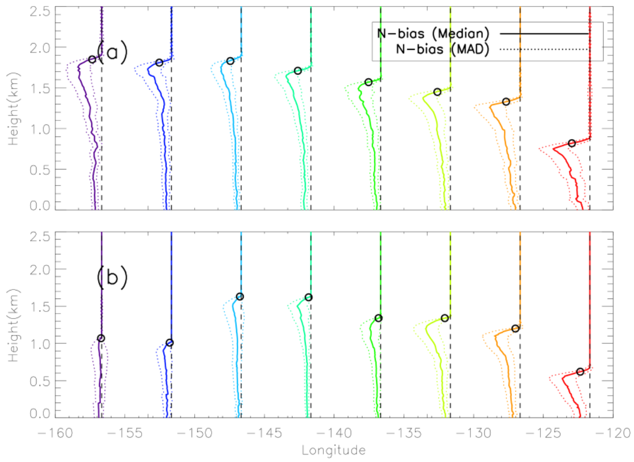

Figure 8: Median *N*-bias (solid) ± MAD (dotted) along the north Pacific transect for MAGIC radiosondes (a) and ERA5 (b). Open circles represent the median ~~PBL height~~PBLH for each 5° bin.

Formatted: Font: Italic

Table 1: ~~5° bin median~~Median and MAD peak *N*-bias values for MAGIC radiosondes (RDS) and ERA5 for each 5° bin.

Formatted: Font: Italic

Peak N-bias				
Longitude	RDS median	RDS MAD	ERA5 median	ERA5 MAD
-157.5°	-6.11	±2.85	-0.71	±1.80
-152.5°	-5.24	±2.91	-2.23	±1.68
-147.5°	-4.85	±2.18	-2.03	±2.25
-142.5°	-5.78	±2.44	-3.10	±2.24
-137.5°	-5.34	±2.95	-2.60	±2.21
-132.5°	-5.92	±3.14	-5.41	±2.79
-127.5°	-6.42	±3.38	-5.60	±2.74
-122.5°	-8.10	±3.27	-6.23	±2.98

Peak N-bias				
Longitude	**RDS median**	**RDS MAD**	**ERA5 median**	**ERA5 MAD**
−157.5°	−5.12	±2.61	−0.77	±1.73
−152.5°	−5.10	±2.97	−1.76	±1.61
−147.5°	−4.37	±2.14	−1.83	±2.10
−142.5°	−5.36	±2.53	−2.95	±2.17
−137.5°	−4.82	±2.96	−2.31	±2.14
−132.5°	−5.90	±3.03	−5.31	±2.68
−127.5°	−6.55	±3.40	−5.45	±2.88
−122.5°	−7.86	±3.15	−5.92	±3.04

Figure 9 further illustrates the peak *N*-bias, median PBL *N*-bias (0.3 km to PBLH), and the near surface *N*-bias (at 0.3 km) at each bin along the transect. Note~~ that~~ the ~~quality control process removes the refractivity profiles below 0.3 km. Therefore, the median N-bias is the ~~median PBL *N*-bias refer to the median value from the near surface (0.3 km) to the PBLH.

Contrary to the general trend of westward decrease in magnitude of the minimum ~~N-~~refractivity gradient (Fig. 4b) and ducting strength (Fig. 5c), the radiosonde peak *N*-bias shows the maximum (median: ~~–~~–8.10%, MAD: 3.26%) near California ~~(~~(–122.~~5°~~5˚E) and the minimum (median: ~~–~~–4.85%, MAD: 2.18%) over the transition region ~~(~~(–147.~~5°~~5˚E) as well as a slight increase to a secondary maximum (median: ~~-~~–6.11%, MAD: 2.85%) near Hawaii ~~(~~(–157.~~5°~~5˚E). The median PBL *N*-bias and the near surface *N*-bias also show a similar pattern. However, the median *N*-bias demonstrates a sharp decrease in the eastern half of the domain from ~~-~~–5.25% (MAD: 2.71%) at ~~-~~–122.~~5°~~5˚E to ~~-~~–1.71% (MAD: 1.26%) at ~~-~~–137.~~5°~~5˚E, and then remains relatively constant over the western half of the domain. Similarly, the near surface *N*-bias reaches a maximum magnitude of ~~-~~–3.54% (MAD: 2.11~~%) and~~%), sharply decreases to ~~-~~–1.06% (MAD: 0.85%) at ~~-~~–137.~~5°~~5˚E, and then remains relatively constant over the western half of the domain.

~~It is important to point out~~Note that ~~the much higher ducting height and larger variation near Hawaii as compared to California leads to smoothed and much smaller median N-gradient values (Fig. 4b), which also results in a smaller~~normalizing each *N*-bias ~~without being normalized~~profile to the PBLH~~.~~ preserves the magnitude of the *N*-bias with various heights. Therefore, the relatively large normalized *N*-bias observed near Hawaii indicates ~~the presence of strong~~more persistent ducting over the trade-cumulus boundary layer regime ~~(Fig. 8a), which will lead to comparable N-bias to that over ~~compared to the ~~stratocumulus-topped PBL.~~transition region in the middle of the transect at -147.5˚E (Fig. 8a).

On the other hand, the ERA5 data show a westward decrease of all three *N*-biases, systematically underestimating all three as compared to the radiosondes. This is expected as the decrease of ERA5 vertical resolution at higher altitude leads to a weaker PBL *N*-gradient observation (Fig. 4b), and thus weaker ducting and a smaller ducting-induced *N*-bias. Such underestimation of the *N*-bias in the ERA5 ~~is at a minimum~~minimizes near California where the PBLH is lowest but becomes more severe westward with an increase in height, reaching a maximum magnitude *N*-bias difference near Hawaii. In this case, the peak *N*-bias is merely ~~-~~–0.71% (MAD: 1.80%) as compared to ~~-~~–6.23% (MAD: 2.98%) at ~~-~~–122.~~5°~~5˚E (Fig. 9a and Table 1). The large difference

Formatted: Font: Italic
Formatted: Font: Italic
Formatted: Font: Italic
Formatted: Font: Italic
Formatted: Font: Italic
Formatted: Font: Italic
Formatted: Font: Italic
Formatted: Font: Italic
Formatted: Font: Italic
Formatted: Font: Italic
Formatted: Font: Italic
Formatted: Font: Italic
Formatted: Font: Italic
Formatted: Font: Italic
Formatted: Font: Italic
Formatted: Font: Italic

seen in the *N*-bias along the transect strongly indicates the challenges of the ERA5 data to resolve the sharp gradient across the ducting layer, resulting in a large variation in PBLH of the ERA5 data in the western segment of the region. The increasing difference between the radiosonde and ERA5 data from east to west is most pronounced in the peak *N*-bias cross-section (Fig. 9a) but is also ~~clearly~~ evident in both the median *N*-bias (Fig. 9b) as well as the near surface *N*-bias (Fig. 9c).

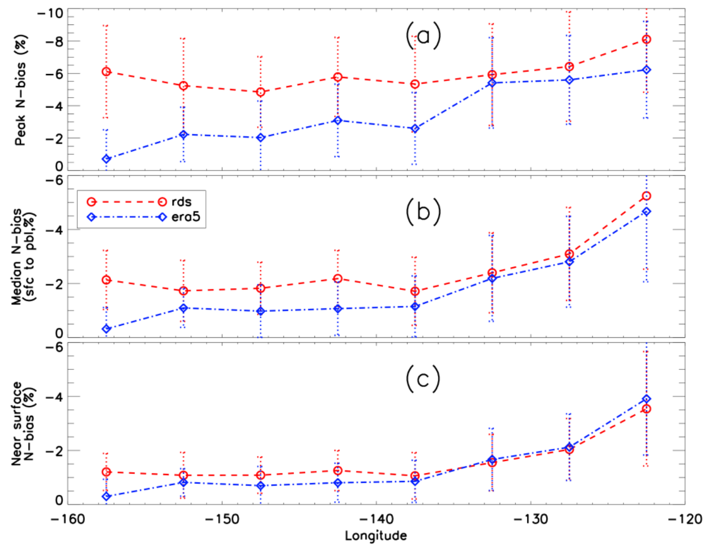

Figure 9: Zonal transect of 5° bin (a) peak *N*-bias, (b) median PBL *N*-bias~~,~~ (0.3 km to PBLH), and (c) near surface *N*-bias at 0.3 km for MAGIC (median in red circle and red-dashed line, MAD in red-dotted error bar) and ERA5 (median in blue diamond and dot-dashed line, MAD in blue-dotted error bar)

3.3.3 The relationship between *N*-bias ~~climatology~~ and key ~~variable analysis~~variables

Figure 10 shows a scatter plot of the PBLH vs. height of ~~maximum~~peak *N*-bias along the transect with each data point colored by the center longitude of the bin to which it belongs. The PBLH and the height of ~~maximum~~peak *N*-bias show a clear linear relationship with high correlation for both the MAGIC (0.89) and ERA5 (0.98) data. The majority of the radiosonde data show the heights of ~~the maximum~~peak *N*-bias ~~aligns~~align well with the PBLH ~~but~~ with a very small low bias (less than ~~70~~80 m). The reason for the lower correlation value ~~when compared to the ERA5~~in MAGIC data is attributed to outlier cases when the radiosonde *N*-bias profiles with a double peak at which the larger magnitude bias is located (Fig. 7a). On the other hand, the ERA5 maximum ducting heights show little difference from the PBLH near California (e.g., -

Formatted: Font: Italic
Formatted: Font: Italic
Formatted: Font: Italic
Formatted: Font: Italic
Formatted: Font: Italic
Formatted: Font: Italic
Formatted: Font: Italic
Formatted: Font: Italic
Formatted: Font: Italic
Formatted: Font: Italic
Formatted: Font: Italic
Formatted: Font: Italic

~~−~~122.~~5~~5°E), but become lower moving westward, which is illustrated by the increasing difference between the linear regression line and the 1:1 line.

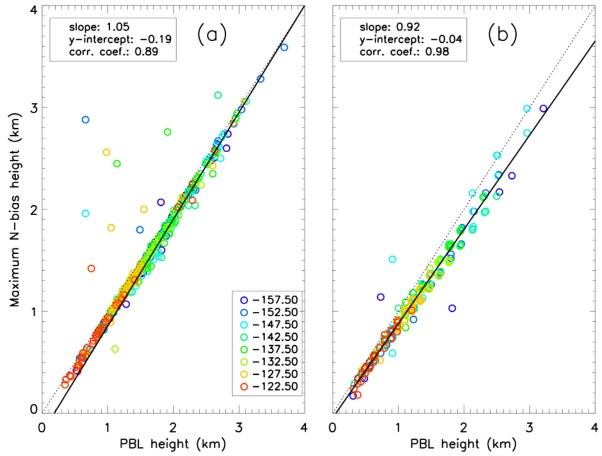

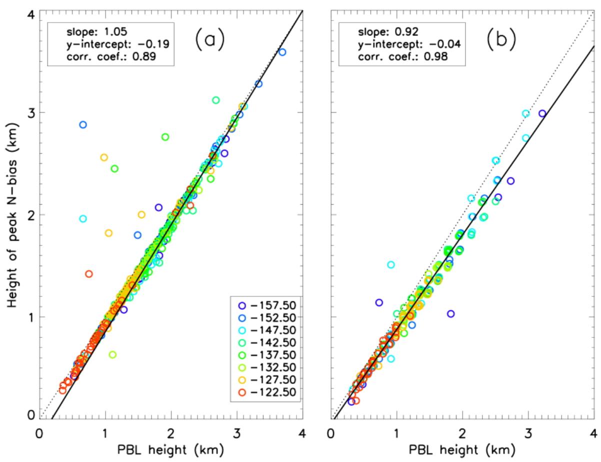

Figure 10: PBLH vs. height of ~~maximum~~peak *N*-bias for individual profiles from MAGIC (a) and ERA5 (b) data. ~~Color~~The color of each open circle ~~represent~~represents the center longitude of the 5° bin to which each profile belongs.

Figure 11 shows ~~the minimum refractivity gradient as a function of ducting-induced refractivity bias for MAGIC radiosondes (a) and ERA5 (b) and the corresponding sharpness parameters (c) and (d), respectively. A~~a near-linear relationship between the minimum refractivity gradients and the ~~maximum~~peak *N*-biases ~~is evident~~ for both MAGIC radiosondes and ERA5 profiles~~; in other words,~~, i.e., the sharper the ~~N~~ refractivity gradient, the larger the *N*-bias. ~~The linear fit function~~

Formatted: Font: Italic

Formatted: Font: 9 pt, Bold

Formatted: Justified, Line spacing: single

Formatted: Font: Italic

Formatted: Font: Italic

~~along with the~~The correlation coefficient for both MAGIC radiosondes (0.93) and the ERA5 profiles (0.88) are also presented.

The sharpness parameter (Fig. 11c, 11d) also shows a linear relationship with the maximum *N*-bias which is a result of its dependence on the minimum ~~N-gradient. While a similar conclusion can be reached, it is interesting to note that the difference in the correlation of the radiosonde (-0.83) and the ERA5 (-0.84) does not lie in the observations with the larger magnitude peak N-bias, but in those closer to zero as the radiosonde data clearly centers below the regression line and trends above while the ERA5 with peak N-bias less than 5% are centered around the regression line. In the case of both key variables~~refractivity gradient. Interestingly, their relationship with the peak *N*-bias exhibits no indication of zonal dependence.

Formatted: Font: Italic

Formatted: Font: Italic

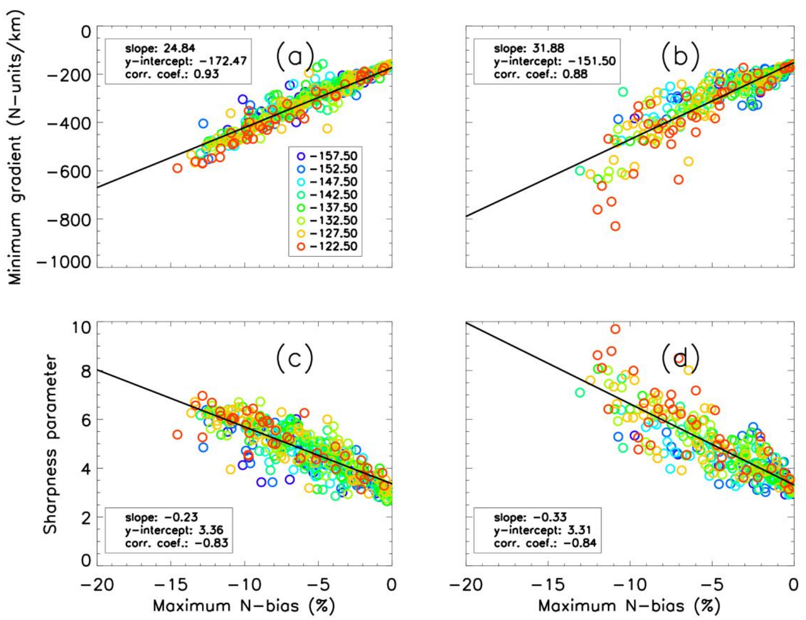

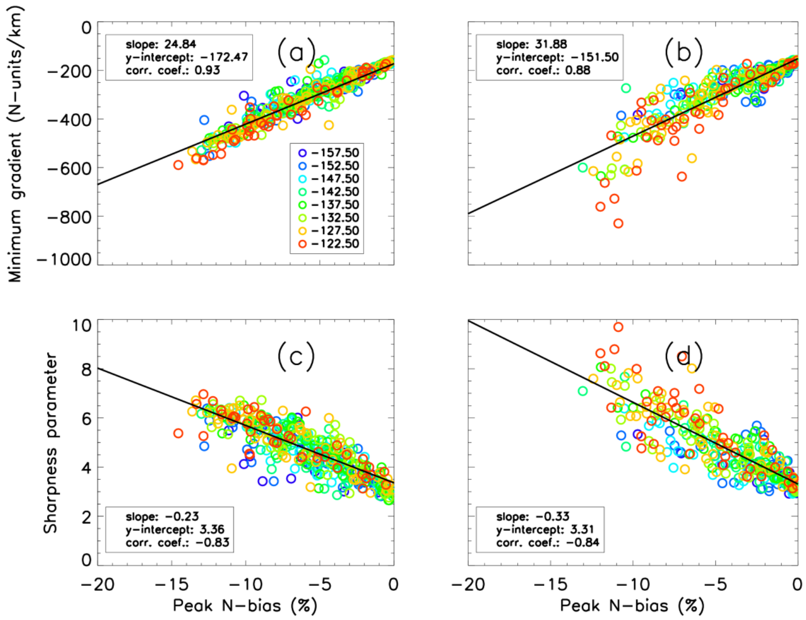

Figure 11: (a, b) Minimum refractivity gradient (N-units km^{-1}) and (c, d) sharpness parameter, as a function of the ~~maximum~~peak *N*-bias (%) for MAGIC (a, c) and ERA5 (b, d) data with the line of linear regression in solid black. Color of each open circle represents the center longitude of the 5° bin to which each profile belongs.

4 4 Summary and Conclusions

In this study, radiosonde profiles from the MAGIC field campaign have been analyzed to investigate ~~the~~ ducting ~~climatology~~characteristics and the ~~impact of associated~~induced systematic refractivity biases ~~that occur~~in GNSS RO retrievals over the ~~eastern North~~Northeastern Pacific Ocean between Hawaii and California. Colocated ERA5 model reanalysis data were used as a secondary comparison to the radiosonde observations.

The nearly 1-year high-resolution MAGIC radiosonde dataset reveals the frequent presence of ducting ~~at a well-defined PBL throughout the transect~~ marked by a sharp refractivity gradient resulting from the large moisture lapse rate across a strong temperature inversion layer. The PBLH increases by more than 1 km along the transect from ~~CA~~California to ~~HI~~Hawaii while the magnitude of the ~~N~~ refractivity gradient decreases by 100 N-units km^{-1}. The zonal gradient of both variables illustrates the transition of the PBL from shallow stratocumulus adjacent to the California coast to deeper trade-wind cumulus that are prevalent near the Hawaiian Islands.

Formatted: Font: Italic

Formatted: Normal, No bullets or numbering

Formatted: Font: Times New Roman, 12 pt, Bold

~~To~~End-to-end simulation on all radiosonde and ERA5 refractivity profiles has been conducted to estimate the systematic negative *N*-bias in GNSS RO observations~~ due to ducting, we applied an end-to-end simulation on all radiosonde refractivity profiles that contained at least one elevated ducting layer.~~. The ducting layer ~~thickness remained~~maintains remarkably consistent thickness (110 m) ~~across~~along the transect with westward decreasing strength and increasing height. The ERA5 slightly underestimates both the height and strength of the ducting layer ~~and so~~as well as the PBLH.

~~The maximum N-~~A systematic negative refractivity bias ~~occurs just~~(*N*-bias) below the ~~PBLH, where the refractivity gradient~~ ducting layer is ~~strongest.~~observed throughout the transect, peaking (−5.42%) approximately 80 meters below the PBL height, and gradually decreasing towards the surface (−0.5%). The height of the ~~maximum~~peak *N*-bias and the PBLH show a highly positive correlation. The ~~mean~~median difference between the two is about ~~70~~80 meters in the radiosonde but increasing to about 120 meters in the colocated ERA5 data. ~~The correlation between the PBLH and the height of the maximum N-bias is highly positive.~~

MAGIC radiosondes ~~indicated~~indicate larger values of both ducting strength (ΔN) and thickness (Δh) than ~~from~~ ERA5 in the western half of the transect. The ~~reverse~~opposite is true in the eastern portion of the domain, and is likely associated with the transition of the cloud layer from open-cell cumulus in the west to stratocumulus and stratus in the east (~~Wood et al., 2015;~~ Bretherton et al., 2019~~). While this segment of the transect also coincides with a better sampling rate for the~~; Wood et al., 2011). The ERA5 ~~data (~40 m vertical resolution), the ERA5 continues to~~ systematically ~~underestimate~~underestimates the average ducting layer gradient ~~climatology~~ ($\Delta N/\Delta h$) ~~when compared~~comparing to the radiosondes. The largest *N*-bias is ~~located in~~found over the region ~~of~~with strongest ducting ~~which also corresponds to the~~ and largest sharpness parameter. It is worth noting that the PBL over the western portion of the transect near Hawaii frequently shows two major gradient layers (a mixing layer at ~1 km and the trade-inversion at ~2 km), with comparable *N*-gradients (e.g., Fig. ~~The limited~~2). The much lower PBLH seen in ERA5 in this region is likely due, in part, to the decreasing number of model levels in ERA5 ~~near 2 km causes ducting to be underrepresented near the trade wind inversion which is evident in~~ at higher altitude, which could lead to higher possibility of identifying the ~~discrepancy between~~lower gradient layer as the ~~radiosonde and ERA5 PBLH cross sections~~PBLH. However,

Formatted: Font: Italic

Formatted: Font: Italic

Formatted: Font: Italic

the impact of the vertical resolution on the performance of gradient method for PBLH detection has not been performed in this study and warrants more comprehensive study in the future. Future work will include a comprehensive simulation study to explore the regional difference in horizontal inhomogeneity and its impact on GNSS RO soundings. This research will improve RO data quality, enhance understanding of PBL inhomogeneity, and advances weather and climate prediction capabilities.

5 5 Data availability

Formatted: Normal, No bullets or numbering

Data for the Marine Atmospheric Radiation Measurement (ARM) GCSS Pacific Cross Section Intercomparison (GPCI) Investigation of Clouds (MAGIC, Zhou et al.., 2015) can be accessed through the U.S. Department of Energy's Office of Science https://www.arm.gov/research/campaigns/amf2012magic.

Data for the ECMWF Reanalysis version 5 (ERA5, Hersbach et al.., 2020) can be accessed at https://www.ecmwf.int/en/forecasts/dataset/ecmwf-reanalysis-v5.

Formatted: Normal, No bullets or numbering

~~6~~ 6 Author contribution

Author Thomas Winning is responsible for all original text and, data analysis and production of graphics. Author Kevin Nelson contributed by providing updated data processing code, colocation of ERA5 data with MAGIC observations and first and second round edits. Author Feiqin Xie is the academic advisor for the primary author and also provided draft edits and paper organization and writing guidance.

7 Competing interests

The authors declare no competing interests, see Acknowledgements for current affiliation.

Formatted: Normal, No bullets or numbering

~~7~~ 8 Acknowledgements

The authors acknowledge funding support of earlier work from NASA grant (NNX15AQ17G). Authors T. Winning and K. Nelson were also partially supported by research assistantship from Coastal Marine System Science Program at Texas A&M University – Corpus Christi. The high-resolution ERA5 reanalysis data were acquired from ECMWF~~.~~ and the Climate Data Service (CDS). The MAGIC radiosonde data were provided by the Atmospheric Radiation Measurement program (ARM) Climate Research Facility sponsored by the U.S. Department of Energy (DOE). Author T. Winning's current affiliation: Ventura County Air Pollution Control District, Ventura, CA, 93003, USA. Author T. Winning acknowledges this work was done as ~~a private venture~~an academic pursuit in association with Texas A&M University – Corpus Christi and not in the author's capacity as an employee of the Ventura County Air Pollution Control District.
Author K. Nelson's current affiliation: Jet Propulsion Laboratory, California Institute of Technology, Pasadena, CA, 91109, USA. Author K. Nelson acknowledges this work was done as a private venture and not in the ~~authors'~~author's capacity as an employee of the Jet Propulsion Laboratory, California Institute of Technology.

Formatted: Pattern: Clear (White)

References

Anthes, R. A., and Coauthors: The COSMIC/FORMOSAT-3 Mission: Early Results, BAMS, 89, 313–334, doi.org/10.1175/bams-89-3-313, 2008.

Ao, C. O., Meehan T. K., Hajj, G. A., Mannucci, A. J., and Beyerle, G.: Lower Troposphere Refractivity Bias in GPS Occultation Retrievals, J. Geophys. Res., 108, 4577, doi:10.1029/2002JD003216, 2003.

Ao, C. O.: Effect of Ducting on Radio Occultation Measurements: An Assessment Based on High-resolution Radiosonde Soundings, Radio Sci., 42, RS2008, doi.org/10.1029/2006RS003485, 2007.

Ao, C. O., Chan, T. K., Iijima, A., Li, J.-L., Mannucci, A. J., Teixeira, J., Tian, B., and Waliser, D. E.: Planetary Boundary Layer Information from GPS Radio Occultation Measurements, in: Proceedings of the GRAS SAF Workshop on Applications of GPSRO Measurements, Vol. 5 of, GRAS SAF Workshop on Applications of GPSRO Measurements, Reading, United Kingdom, ECMWF and EUMETSAT, 123–131, https://www.ecmwf.int/sites/default/files/elibrary/2008/7459-planetary-boundary-layer-information-gps-radio-occultation-measurements.pdf, 16-–18 June, 2008.

Ao, C. O., Waliser, D. E., Chan, S. K., Li, J.-L., Tian, B., Xie, F., and Mannucci, A. J.: Planetary boundary layer heights from GPS radio occultation refractivity and humidity profiles, J. Geophys. Res., 117, D16117, doi:10.1029/2012JD017598, 2012.

Basha, G., and Ratnam, M. V.: Identification of atmospheric boundary layer height over a tropical station using high-resolution radiosonde refractivity profiles: Comparison with GPS radio occultation measurements, J. Geophys. Res., 114, doi.org/10.1029/2008jd011692, 2009.

Beyerle, G., Gorbunov, M. E., and Ao, C.O.: Simulation studies of GPS radio occultation measurements, Radio Sci., 38, 1084, doi:10.1029/2002RS002800, 2003.

Bretherton, C.S., and Coauthors: Cloud, Aerosol, and Boundary Layer Structure across the Northeast Pacific Stratocumulus-–Cumulus Transition as Observed during CSET, Mon.Wea. Rev., 147, 2083-–2102. DOI: 10.1175/MWR-D-18-0281, 2019

Eshleman, V.R.: The radio occultation method for the study of planetary atmospheres, Planet. Space Sci., 21, 1521-1531, doi.org/10.1016/0032-0633(73)90059-7, 1973.

Feng, X., Xie, F., Ao, C.O., and Anthes, R.A.: Ducting and Biases of GPS Radio Occultation Bending Angle and Refractivity in the Moist Lower Troposphere, J. Atmos. Oceanic Technol., 37, 1013–1025, doi.org/10.1175/~~JTECHJTECH~~JTECH-D-19-0206.1, 2020.

Fjeldbo, G., and Eshleman, V.R.: The Atmosphere of Mars Analyzed by Integral Inversion of the Mariner IV Occultation Data, Planet. Space Sci., 16, 1035-1059, doi.org/10.1016/0032-0633(68)90020-2, 1968.

Fjeldbo, G., Kliore, A.J., and Eshleman, V.R.: The Neutral Atmosphere of Venus as Studied with the Mariner V Radio Occultation Experiment, Astron. J., 76, 123-140, doi.org/10.1086/111096, 1971.

Garratt, J. R.: Review: the atmospheric boundary layer, Earth-Sci. Rev., 37, 89–134, 1994

Guo, P., Kuo, Y. H., Sokolovskiy, S. V., and Lenschow, D. H.: Estimating Atmospheric Boundary Layer Depth Using COSMIC Radio Occultation Data, J. Atmos. Sci., 68, 1703–1713, doi.org/10.1175/2011jas3612.1, 2011.

Gorbunov, M. E.: Canonical transform method for processing radio occultation data in the lower troposphere, Radio Sci., 37(5), 1076, doi:10.1029/2000RS002592, 2002.

Gorbunov, M. E., Benzon, H. H., Jensen, A.S, Lohmann, M.S., and Nielsen, A.S.: Comparative analysis of radio occultation processing approaches based on Fourier integral operators. Radio Sci., 39, RS6004, https://doi.org/10.1029/2003RS002916, 2004

Healy, S. B.: Radio occultation bending angle and impact parameter errors caused by horizontal refractive index gradients in the troposphere: A simulation study, J. Geophys. Res, 106, D11, 11875–11889, doi:10.1029/2001JD900050, 2001.

Hersbach, H., Bell, B., Berrisford, P., Hirahara, S., Horányi, A., Muñoz-Sabater, J., Nicolas, J., Peubey, C., Radu, R., Schepers, D., Simmons, A., Soci, C., Abdalla, S., Abellan, X., Balsamo, G., Bechtold, P., Biavati, G., Bidlot, J., Bonavita, M., De Chiara, G., Dahlgren, P., Dee, D., Diamantakis, M., Dragani, R., Flemming, J., Forbes, R., Fuentes, M., Geer, A., Haimberger, L., Healy, S., Hogan, R. J., Hólm, E., Janisková, M., Keeley, S., Laloyaux, P., Lopez, P., Lupu, C., Radnoti, G., de Rosnay, P., Rozum, I., Vamborg, F., Villaume, S., and ~~Coauthors~~Thépaut, J.-N.: The ERA5 Global Reanalysis, ~~Quart~~Q. J. Roy. Meteor. Soc., 146, 1999–2049, https://doi~~:~~.org/10.1002/qj.3803, 2020.

Ho, S.-P., Peng, L., Anthes, R. A., Kuo, Y.-H., and Lin, H.-C.: Marine boundary layer heights and their longitudinal, diurnal and inter-seasonal variability in the southeast Pacific using COSMIC, CALIOP, and radiosonde data. J. Climate, 28, 2856–2872, https://doi.org/10.1175/JCLI-D-14-00238.1, 2015.

Formatted: Normal (Web), Left, Line spacing: single

Formatted: Don't adjust space between Latin and Asian text, Don't adjust space between Asian text and numbers

Formatted: Left, Line spacing: single, Don't adjust space between Latin and Asian text, Don't adjust space between Asian text and numbers

Jensen, A. S., Lohmann, M.S., Nielsen, A.S. and Benzon, H.-H.: Geometrical optics phase matching of radio occultation signals, Radio Sci., 39, RS3009, doi:10.1029/2003RS002899, 2004.

Jensen, A. S., Lohmann, M.S., Benzon, H.-H, and Nielsen, A.S.: Full spectrum ~~inverstion~~inversion of radio occultation signals, Radio Sci., 38(3), 1040, doi:10.1029/2002RS002763, 2003.

Johnston, B. R., Xie, F., and Liu, C.: The effects of deep convection on regional temperature structure in the tropical upper troposphere and lower stratosphere, J. Geophys. Res.: Atmos., 123, 1585–1603, doi.org/10.1002/2017JD027120, 2018.

Klein, S. A., and Hartmann, D. L.: The seasonal cycle of low stratiform clouds. Journal of Climate, 6, 1587–1606, doi:10.1175/1520-0442(1993)006<1587:TSCOLS>2.0.CO;2, 1993.

Kursinski, E. R., Hajj, G. A., Schofield, J. T., Linfield, R. P., and Hardy, K. R.: Observing Earth's atmosphere with radio occultation measurements using the Global Positioning System, J. Geophys. Res.: Atmos., 102, 23429–23465, doi.org/10.1029/97jd01569, 1997.

Kursinski, E. R., G. A. Hajj, Leroy, S. S., and Herman, B.: The GPS Radio Occultation Technique. Terr. Atmos. Ocean. Sci. (TAO), 11, 53–114, 2000.

Lewis, E. R.: Marine ARM GPCI Investigation of Clouds (MAGIC) Field Campaign Report. U.S. Department of Energy, https://doi.org/10.2172/1343577, 2016.

Maddy, E. S. and Barnet, C. D.: Vertical resolution estimates in version 5 of AIRS operational retrievals. IEEE Transactions on Geoscience and Remote Sensing, 46, 2375–2384, doi:10.1109/TGRS.2008.917498, 2008.

Nelson, K. J., Xie, F., Ao, C. O., and Oyola-Merced, M. I.: Diurnal Variation of the Planetary Boundary Layer Height Observed from GNSS Radio Occultation and Radiosonde Soundings over the Southern Great Plains. J. Atmos. Oceanic Tech., 38, 2081–2093, https://doi.org/10.1175/jtech-d-20-0196.1, 2021.

Nelson, K. J., Xie, F., Chan, B. C., Goel, A., Kosh, J., Reid, T. G. R., Snyder, C. R., and Tarantino, P. M.: GNSS Radio Occultation Soundings from Commercial Off-the-Shelf Receivers Onboard Balloon Platforms, Atmos. Meas. Tech., https://doi.org/10.5194/amt-2022-198, 2022.

Painemal, D., Minnis, P., and Nordeen, M.: Aerosol variability, synoptic-scale processes, and their link to the cloud microphysics over the northeast Pacific during MAGIC, J. Geophys. Res. Atmos., 120, 5122–5139, doi:10.1002/2015JD023175, 2015.

Formatted: Font: Not Italic

Formatted: Font: Not Bold

Formatted: Font: +Body (Calibri), 11 pt

Formatted: Font: +Body (Calibri), 11 pt

Patterson, W. L.: Climatology of Marine Atmospheric Refractive Effects: A Compendium of the Integrated Refractive Effects Prediction System (IREPS) Historical Summaries. Naval Ocean Systems Center, https://apps.dtic.mil/sti/pdfs/ADA155241.pdf, 1982.

Ramanathan, V., Cess, R. D., Harrison, E. F., Minnis, P., Barkstrom, B. R., Ahmad, E., and Hartmann, D.: Cloud-radiative forcing and climate: Results from the Earth Radiation Budget Experiment, Science, 243, 57–63, DOI:10.1126/science.243.4887.57, 1989.

Riehl, H.: Climate and weather in the tropics. London: Academic Press. 611 pp. ISBN 0.12.588180.0

Rocken, C., Anthes, R., Exner, M., Hunt, D., Sokolovskiy, S., Ware, R., Gorbunov, M., Schreiner, W., Feng D., Herman B., Kuo, Y.-H., Zou, X.: Analysis and validation of GPS/MET data in the neutral atmosphere. J. Geophys. Res., 102, 29849–29866, https://doi.org/10.1029/97JD02400, 1997.

Schreiner, W. S., Weiss, J.P., Anthes, R.A., Braun, J., Chu, V., Fong, J., Hunt, D., Kuo, Y.-H., Meehan, T., Serafino, W., Sjoberg, J., Sokolovskiy, C., Talaat, E., Wee, T.K., Zeng, Z.: COSMIC-2 Radio Occultation Constellation: First Results. Geophys. Res. Lett., 47, https://doi.org/10.1029/2019gl086841, 2020.

Seidel, D. J., Ao, C.O. and Li, K.: Estimating climatological planetary boundary layer heights from radiosonde observations: Comparison of methods and uncertainty analysis, J. Geophys. Res., 115, D16114, doi:10.1029/2009JD013680, 2010.

Smith, E. K. and Weintraub, S.: The Constants in the Equation for Atmospheric Refractivity Index at Radio Frequencies. Proc. IRE, 41, 1035–1037, doi:10.1109/JRPROC.1953.274297, 1953.

Sokolovskiy, S. V.: Modeling and Inverting Radio Occultation Signals in the Moist Troposphere. Radio Sci., 36, 441–458, https://doi.org/10.1029/1999RS002273, 2001.

Sokolovskiy, S. V.: Effect of super refraction on inversions of radio occultation signals in the lower troposphere. Radio Sci., 38 (3), https://doi.org/10.1029/2002RS002728, 2003.

Sokolovskiy, S. V., Kuo, Y.-H., Rocken, C., Schreiner, W. S., Hunt, D. and Anthes, R. A., 2006: Monitoring the atmospheric boundary layer by GPS radio occultation signals recorded in the open-loop mode. Geophys. Res. Lett., 33, L12813, doi:10.1029/2006GL025955, 2006.

Formatted: Font: +Body (Calibri), 11 pt

Formatted: Heading 2, Left, Pattern: Clear (White)

Formatted: Font: +Body (Calibri), 11 pt

Stull, R., Santoso, E., Berg, L. K., and Hacker, J.: Boundary Layer Experiment 1996 (BLX96), BAMS, 78, 1149–1158, doi: 10.1175/1520-0477(1997)078<1149:BLEB>2.0.CO;2, 1997.

Stull, R. B.: An Introduction to Boundary Layer Meteorology. Kluwer Academic Publishers, 666 pp., ISBN 90-277-2768-6, 1988.

von Engeln, A. and Teixeira, J.: A Planetary Boundary Layer Height Climatology Derived from ECMWF Reanalysis Data, J. Climate, 26, 6575–6590, https://doi.org/10.1175/jcli-d-12-00385.1, 2013.

Winning, T. E., Chen, Y.-L., and Xie, F.: Estimation of the marine boundary layer height over the central North Pacific using GPS radio occultation, Atmospheric Research, 183, 362–370, https://doi.org/10.1016/j.atmosres.2016.08.005, 2017.

Wood, R., Mechoso, C. R., Bretherton, C. S., Weller, R. A., Huebert, B., Straneo, F., Albrecht, B. A., ~~…, Bower, K.~~ Coe, H., Allen, G., Vaughan, G., Daum, P., Fairall, C., Chand, D., Gallardo Klenner, L., Garreaud, R., Grados, C., Covert, D. S., Bates, T. S., Krejci, R., Russell, L. M., de Szoeke, S., Brewer, A., Yuter, S. E., Springston, S. R., Chaigneau, A., Toniazzo, T., Minnis, P., Palikonda, R., Abel, S. J., Brown, W. O. J., Williams, S., Fochesatto, J., Brioude, J., and Bower, K. N.: The VAMOS Ocean-Cloud-Atmosphere-Land Study Regional Experiment (VOCALS-REx): goals, platforms, and field operations, Atmos. Chem. Phys., 11, 627–654, https://doi.org/10.5194/acp-11-627-2011, 2011.

~~Wood, R., Wyant, M., Bretherton, C. S., Rémillard, J., Kollias, P., Fletcher, J., … Lin, Y.: Clouds, aerosols, and precipitation in the Marine Boundary Layer: An ARM Mobile Facility deployment. BAMS, 96, 419-440. doi:10.1175/BAMS-D-13-00180.1, 2015.~~

Xie, F., Syndergaard, S., Kursinski, E. R., and Herman, B.M.: An Approach for Retrieving Marine Boundary Layer Refractivity from GPS Occultation Data in the Presence of Super-refraction. J. Atmos. Oceanic Technol., 23, 1629–1644, https://doi.org/10.1175/JTECH1996.1, 2006.

Xie, F., Haase, J. S., and Syndergaard, S.: Profiling the Atmosphere Using the Airborne GPS Radio Occultation Technique: A Sensitivity Study. IEEE Transactions on Geoscience and Remote Sensing, 46, 3424–3435, https://doi.org/10.1109/tgrs.2008.2004713, 2008.

Xie, F., Wu, D. L., Ao, C. O., Kursinski, E. R., Mannucci, A. J., and Syndergaard, S.: Super-refraction effects on GPS radio occultation refractivity in marine boundary layers, Geophys. Res. Lett., 37, https://doi.org/10.1029/2010gl043299, 2010.

Formatted: Font: 8 pt, Font color: Auto

Formatted: Font: Not Italic

Formatted: Font: Not Bold

Xie, F., Wu, D. L., Ao, C. O., Mannucci, A. J., and Kursinski, E. R.: Advances and limitations of atmospheric boundary layer observations with GPS occultation over southeast Pacific Ocean, Atmos. Chem. Phys., 12, 903–918, doi:10.5194/acp-12-903-2012, 2012.

Zhou, X., Kollias, P., and Lewis, E.: Clouds, precipitation and marine boundary layer structure during MAGIC. J. Climate, 28, 2420–2442, https://doi.org/10.1175/JCLI-D-14-00320.1, 2015.